Probing Dark Current Random Telegraph Signal in a Small Pitch Vertically Pinned Photodiode CMOS Image Sensor after Proton Irradiation

Aubin Antonsanti, *Student Member, IEEE*, Cédric Virmontois, *Member, IEEE*,
Jean-Marie Lauenstein, *Member, IEEE*, Alexandre Le Roch, *Member, IEEE*,
Hugo Dewitte, *Student Member, IEEE*, Vincent Goiffon, *Senior Member, IEEE*

Abstract—Dark Current degradation and Dark Current Random Telegraph Signal after proton irradiation are studied in new scale silicon microvolumes by using a commercial CMOS Image Sensor. Results show that previously reported empirical models describing the Displacement Damage induced degradations are still valid despite the 10 to 100 times smaller depletion volume used. In addition, no evidence of significant Total Ionizing Dose effects is observed. Finally the reduction of the fraction of Random Telegraph Signal (RTS) pixels detected and of the fraction of multi-level RTS pixels is directly linked to the reduction in pixel volume.

Index Terms—CMOS Image Sensor (CIS), Displacement Damage Dose (DDD), Dark Current Random-Telegraph-Signal (DC-RTS), Pinned Photodiode (PPD)

I. INTRODUCTION

RADIATION environments often limit the use of high-end solid-state image sensors for space or nuclear applications. In such environments, particles are likely to degrade the sensor's performance. In addition to ionizing dose deposition, displacement damage refers to an impinging particle knocking a target atom out of its position in the crystal lattice of the sensor's photosensitive element. Such damage is known to increase pixels' dark-current, creating an exponentially distributed tail of "hot" pixels. The dynamic range of such hot pixels can be dramatically reduced, up to the point that a pixel may become totally inoperable. Because of displacement damage, some pixels will also start to exhibit a Random Telegraph Signal (RTS), or "blinking", behavior [1], [2]. Dark Current RTS (DC-RTS) pixels see their dark current randomly and instantaneously switch between two or more discrete levels. Image Sensors designed for space applications are sensitive to this RTS behavior as it can disrupt the functioning of scientific instruments and satellites' star-trackers because hot pixels can be mistaken for stars [3] and that the random nature of RTS makes in-flight calibration very hard to perform.

A. Antonsanti, H. Dewitte and V. Goiffon are with ISAE-SUPAERO, Université de Toulouse, 10 avenue E. Belin, F-31055, Toulouse, France (e-mail: aubin.antonsanti@isae.fr).

J. M. Lauenstein is with NASA Goddard Space Flight Center (NASA GSFC), 8800 Greenbelt Rd, Greenbelt, MD 20771, USA (e-mail: jean.m.lauenstein@nasa.gov).

A. Le Roch is with NASA Postdoctoral Program (NPP) at NASA Goddard Space Flight Center (NASA GSFC), 8800 Greenbelt Rd, Greenbelt, MD 20771, USA (e-mail: alexandre.leroch@nasa.gov).

C. Virmontois is with Centre National d'Études Spatiales (CNES), 31400 Toulouse, France (e-mail: cedric.virmontois@cnes.fr).

The purpose of this work is to extend the understanding of dark current and DC-RTS after irradiation using a very small pixel pitch CMOS Image Sensor (CIS). Using such pixels allows sampling the silicon at a new scale in order to verify if the previously reported empirical models in larger pixel CIS are still valid at this scale or if new effects arise. In section II, the device under test and the irradiation conditions are detailed. Section III addresses the evolution of the dark current with the displacement damage dose. The remaining section focuses on the DC-RTS study of the irradiated sensors.

II. EXPERIMENTAL DETAILS

A. Device information

Space agencies are integrating more and more Commercial Off The Shelf (COTS) image sensors in their missions. COTS image sensors enable cost reduction, state-of-the-art technology nodes with advanced performances and functions, and faster development in comparison to custom sensors. The device under test in this study is a COTS CIS, the Sony IMX219PQ, integrated on the Raspberry Pi camera V2. This sensor choice has been motivated by the very small pixel pitch and the high number of pixels, allowing both the desired new scale silicon sampling and good statistics. The IMX219PQ is a Back Side Illuminated (BSI) sensor consisting of $3280{\times}2464$ – $1.12\,\mu m$ pitch pixels. In order to obtain such a small pixel pitch while maintaining a good Full-Well Capacity (FWC), avoiding crosstalk, and without losing too much of the sensitive silicon volume, manufacturers have been using several techniques such as increasing the depth of the photodiode by using vertically pinned photodiodes and Deep Trench Isolation (DTI) [4], [5], [6].

The pixel design is depicted in Fig. 1 based on scanning electron microscopy images from [7]. Pixels are made of vertically Pinned Photodiodes (PDD) electrically and optically isolated from each other with DTI. As a first approximation, the sensitive volume of this pixel is considered as the whole silicon volume and equal to $\approx 1.62\,\mu m^3$. This volume is 10 to 100 times smaller than the typically studied depletion volume used in previous displacement damage effect studies.

A top view of the readout stack can also be seen in [7] and allows us to determine the electrical layout of the pixels. It can be seen from Fig. 1 that four PPDs form a subgroup with four Transfer Gates (TG) connecting them to a shared

Sense Node (SN). Two subgroups of PPDs also share the same Reset (RST), Source Follower (SF), and Row Select (SEL) transistors. This pattern allows the use of only 11 transistors for 8 PPDs or 1.375 transistors per PPD, as depicted in Fig. 1. c). This layout, also reported in [4], permits an easy 2×2 pixel binning but complicates the readout of the sensor. As a result, the maximum framerate when performing readout on the whole pixel array without binning is 15 frames per second.

Because the sensor is integrated, the pixel output voltage cannot be measured. Only the Analog to Digital Unit (ADU) values after the 10 bit Analog to Digital Converter (ADC) are accessible. The conversion gain from charges to ADU can still be evaluated and is equal to $0.18\,\mathrm{ADU/e^-}$ [8]. This conversion gain can be tweaked by changing the value of two parameters: the analog and digital gains. Using unitary analog and digital gains, the FWC is never reached. Instead, the maximum measured signal of $5700\,\mathrm{e^-}$ corresponds to the maximum value of 1023 ADU offered by the 10 bits ADC. Regarding the noise, only the full readout chain noise can be measured and is equal to $1.87\,\mathrm{ADU}$ or $10.4\,\mathrm{e^-}$ at room temperature using unitary gain and an exposure time of $100\,\mathrm{ms}$. According to [5], mean dark current should be equal to $6\,\mathrm{e^-/s}$ at $60\,°\mathrm{C}$ and is thus considered negligible at $22\,°\mathrm{C}$.

One drawback of using COTS is that some on-chip signal processing might occur, even on so-called "raw" images. The IMX219PQ has an automatic Optical Black (OB) clamping circuit that uses the mean signal of sixteen rows of masked pixels that do not see light to correct the ADU values of the effective pixels. This circuit shifts the histogram of the ADU values so that the mean value of the masked pixels equals 64 ADU. It means that regardless of the temperature, gain, or integration time, the mean value of the effective pixels in the dark will be equal to 64 ADU. This is a big issue when assessing the dark current before irradiation since the value of the shift is unknown. After irradiation, it only significantly affects pixels that have a low dark current increase or that were not damaged, as shown in section III.

Fig. 1. Simplified illustration of the IMX219PQ pixel's design based on [7].

B. Irradiation campaign

Four groups of sensors were irradiated with $62\,\mathrm{MeV}$ protons on the Light Ion Facility (LIF) beam line of the "Université Catholique de Louvain" in Louvain, Belgium. The irradiation profiles are detailed in Table. I. All sensors were grounded and both effective and masked pixels were exposed to the beam during irradiation at room temperature. Based on the Non-Ionizing Energy Loss (NIEL) of protons from [9], the deposited displacement damage dose ranges from 235 to $2160\,\mathrm{TeV/g\,(Si)}$ with a $5\,\%$ uncertainty due to the beam inhomogeneity. The associated TID, calculated with a LET of $8.39\,\mathrm{MeV.cm^2/g}$ indicated by the facility in [10], is also reported in Table. I. One set of sensors has been irradiated at a ten times lower particle flux at the lowest DDD (sensor LF235) to investigate possible low displacement damage dose-rate effects.
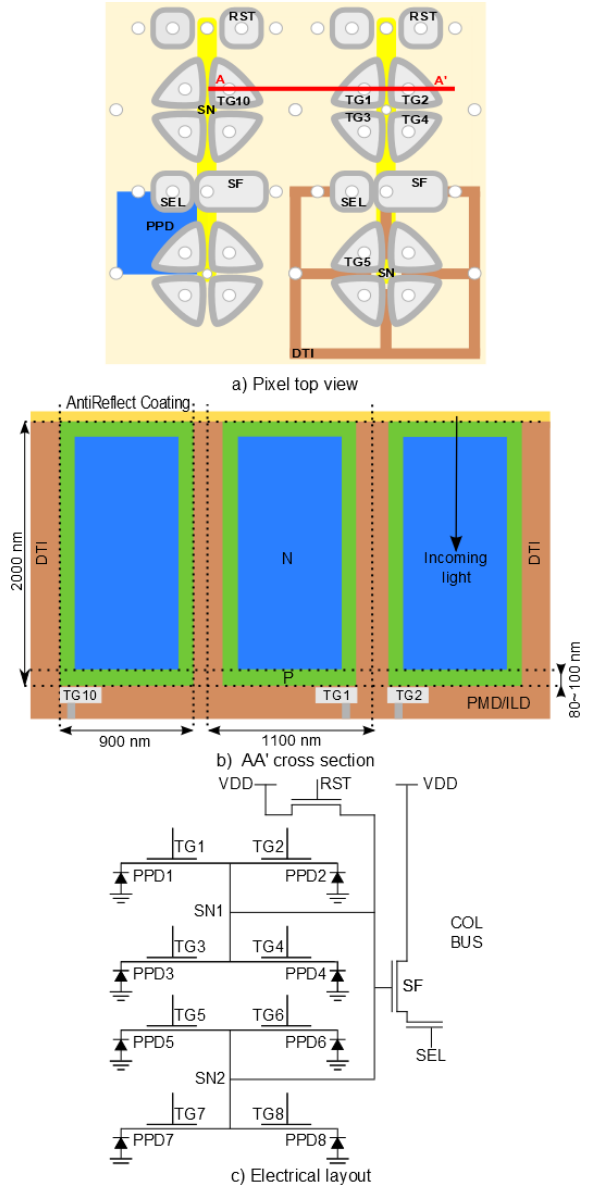
C. Measurements and data processing

DC-RTS measurements of the irradiated sensors were carried out after a storage period of 6 weeks at room temperature ($22\,°\mathrm{C}$). A set of 10 000 images with an integration time of $100\,\mathrm{ms}$ was taken at one frame per second for each sensor. Pixels exhibiting a DC-RTS behavior were detected using the sharp edge detection method presented in [11]. To compensate for a significant self-heating issue, the sensors were placed in a cooled climatic chamber during the measurements. The temperature of the climatic chamber was set to $13.5\,°\mathrm{C}$ so that the stabilized temperature of the sensor measured with a temperature probe reached $22\pm2\,°\mathrm{C}$. Using the same approach, additionnal measurements at 12, 17, 27, and $47\,°\mathrm{C}$ with the same $2\,°\mathrm{C}$ uncertainty were made to extract DC-RTS activation energy. Dark current measurements were made at $22\pm2\,°\mathrm{C}$ after 36 weeks of storage at room temperature.

Sensor	Proton Energy	Proton fluence (p/cm^2)	Proton Flux (p/cm^2/s)	DDD (TeV/g Si)	TID (krad SiO$_2$)
LF235	62 MeV	7.2×10^{10}	2.0×10^7	235	10
HF235	62 MeV	7.2×10^{10}	2.0×10^8	235	10
HF1180	62 MeV	3.6×10^{11}	2.0×10^8	1180	50
HF2160	62 MeV	6.6×10^{11}	2.0×10^8	2160	90

III. DARK CURRENT AFTER IRRADIATION

A. Effect of the black clamping

Because of the black clamping mentioned in section II, extracting the dark current after irradiation is not straightforward. Because masked pixels have also been irradiated, the influence of this correction should be more visible because their mean dark current has increased with the dose. Fig. 2 illustrates the effect of the black clamping at the highest fluence and at room temperature on pixels that have not been damaged by a proton, on pixels with a low dark current increase and, on pixels with a high dark current increase. For undamaged pixels, the successive corrections of 1 ADU between flat portions of the curve are showing that the mean number of collected charges due to dark current in masked pixels is increasing with the integration time, whereas it is not in pixels that are not damaged. The correction is still significant for pixels with a low dark current increase, even though the number of collected charges is slowly increasing with the integration time. However, for pixels with a high dark current increase, the effect of the correction is not visible. Since the object of study here is the exponential tail of pixels with a high dark current induced by displacement damage, the black clamping has a limited impact. It only prevents from evaluating the mean increase of dark current because it is essentially driven by the very high number of pixels that are undamaged or that have a low dark current increase.

B. Displacement Damage induced degradation

Dark current histograms of the irradiated sensors after 36 weeks of annealing at room temperature are shown in Fig. 3 along with the empirical model presented in [12]. No flux effect can be seen when comparing the histograms of sensor L235 and HF235. To predict the shape of the distribution of the dark current after irradiation, the model uses two parameters, ν_{dark}, the mean increase of dark current per displacement damage interaction, and γ_{dark}, a proportionality factor that is used to determine μ_{dark}, the mean number of displacement damage interactions per pixel,

$$\mu_{dark} = \gamma_{dark} V_{dep} DDD, \tag{1}$$

where V_{dep} is the depletion volume of one pixel and DDD the displacement damage dose. If μ_{dark} is small, then the dark current distribution should follow an exponential law

$$f(\Delta I_{dark}) = \frac{1}{\nu_{dark}} \exp(-\frac{\Delta I_{dark}}{\nu_{dark}}). \tag{2}$$
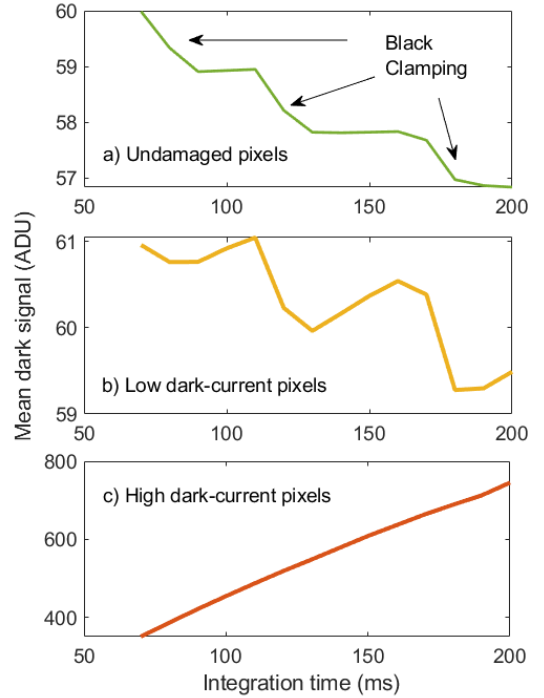

Fig. 2. Evolution of the dark signal of sensor HF2160 with the integration time for a) undamaged pixels, b) pixels with a low dark current increase, c) pixels with a high dark current increase. T=22 °C.

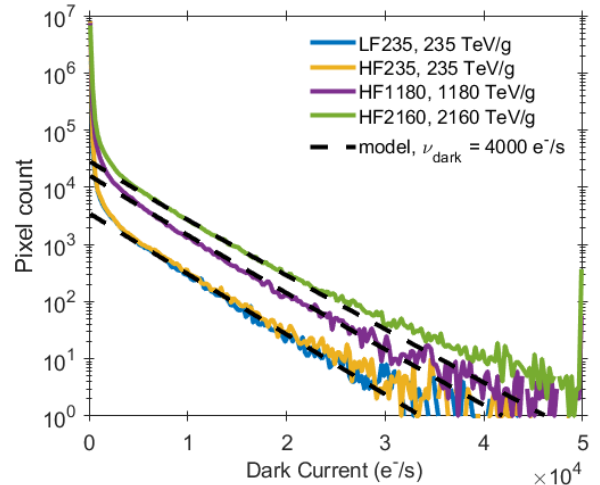Fig. 3. Dark Current histogram of the irradiated sensors at 22°C after 36 weeks of annealing at room temperature.

For greater μ_{dark}, the probability of having multiple interactions per pixel, calculated with the Poisson statistic, needs to be taken into account. The probability of having n displacement interactions knowing μ_{dark} is expressed as

$$\mathcal{P}(n, \mu_{\mathrm{dark}}) = \frac{\mu_{\mathrm{dark}}{}^{n}}{n!} \exp(-\mu_{\mathrm{dark}}) \qquad (3)$$

which is used to evaluate the final distribution,

$$\begin{aligned} F(\Delta I_{\mathrm{dark}}) &= \mathcal{P}(1, \mu_{\mathrm{dark}}) \times f(\Delta I_{\mathrm{dark}}) \\ &+ \mathcal{P}(2, \mu_{\mathrm{dark}}) \times [f(\Delta I_{\mathrm{dark}}) * f(\Delta I_{\mathrm{dark}})] \qquad (4) \\ &+ ... \end{aligned}$$

Finally, the mean increase of dark current due to displacement damage can be retrieved by multiplying (1) by ν_{dark}

$$\Delta\mathrm{I}_{\mathrm{mean,DDD}} = \nu_{\mathrm{dark}}\mu_{\mathrm{dark}} = \nu_{\mathrm{dark}}\gamma_{\mathrm{dark}}\mathrm{V}_{\mathrm{dep}}\mathrm{DDD}. \qquad (5)$$

It is then possible to identify the Universal Damage Factor (UDF) $\mathrm{K}_{\mathrm{dark}}$ introduced in [13] as being the product of the two parameters of the model, ν_{dark} and γ_{dark}

$$\mathrm{K}_{\mathrm{dark}} = \nu_{\mathrm{dark}}\gamma_{\mathrm{dark}}. \qquad (6)$$

Since γ_{dark} represents the number of interactions per unit of volume and dose, only ν_{dark} shares the temperature and annealing time dependency of the UDF [13]. While (6) can be used to reduce the number of degrees of freedom of the model down to a single parameter knowing the value of the UDF, it is not possible to do so here because the black clamping prevents the evaluation of $\Delta\mathrm{I}_{\mathrm{mean,DDD}}$ and then $\mathrm{K}_{\mathrm{dark}}$. Instead, the generic value of $\gamma_{\mathrm{dark}} = 2.4 \times 10^{-5}\,\mu\mathrm{m}^{-3}/(\mathrm{TeV/g})$ [14] that has been found to be independent of the CIS process, pixel pitch, and technology is used to determine μ_{dark} and $\mathrm{K}_{\mathrm{dark}}$, (1) and (6) respectively. The extraction of ν_{dark} is made using the data from sensors LF235 and HF235 because they were exposed to the lowest DDD, ensuring that the slope of their exponential tail of hot pixels in Fig. 3 is a good representation of (2). The best fit is obtained with a depletion volume of $1.28\,\mu\mathrm{m}^{3}$ resulting in a mean dark current increase per displacement damage interaction of $4000\,\mathrm{e}^{-}/\mathrm{s}$ after 36 weeks of annealing at room temperature. The corresponding $\mathrm{K}_{\mathrm{dark}}$ is $0.096\,(\mathrm{e}^{-}/\mathrm{s})/\mu\mathrm{m}^{3}/(\mathrm{TeV/g})$ which once corrected for the temperature and annealing time is very close to the value of the UDF of indicated in [13] (0.21 instead of $0.19\,(\mathrm{e}^{-}/\mathrm{s})/\mu\mathrm{m}^{3}/(\mathrm{TeV/g}))$.

To evaluate the model at higher DDD, every parameter but the DDD is fixed at the value previously reported. Values of μ_{dark}, ν_{dark}, the effective slope considering the first 50 terms of (4), and the mean dark current increase due to DDD are reported in Table II. It is important to notice that even for values of μ_{dark} smaller than 1, (4) leads to an increase of the distribution's exponential slope that is not always negligible. The agreement between the model and the data is very good ($\mathrm{R}^{2} > 0.98$) except for the highest values of dark current that are higher than what is predicted by the model. Electric-Field Enhancement [15] is most likely responsible for this enhancement behavior as also seen for DC-RTS maximum amplitude in section IV.

TABLE II
DARK CURRENT EMPIRICAL MODEL PARAMETERS

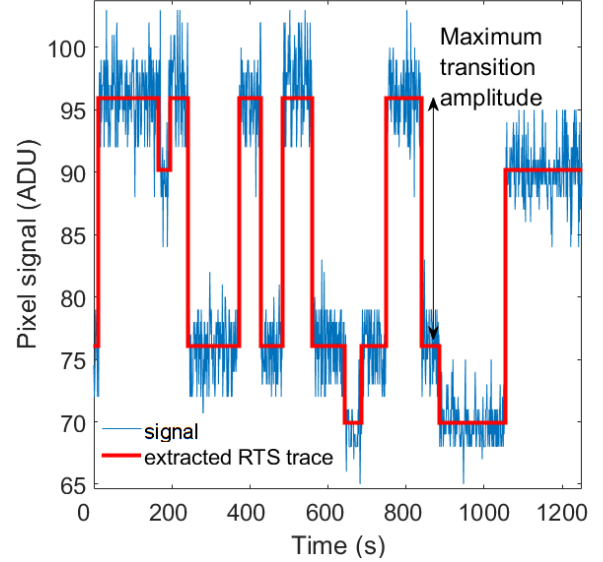| DDD (TeV/g)	μ_{dark}	ν_{dark} ($\mathrm{e}^{-}/\mathrm{s}$)	Effective slope (4) ($\mathrm{e}^{-}/\mathrm{s}$)	$\Delta\mathrm{I}_{\mathrm{mean,DDD}}$ ($\mathrm{e}^{-}/\mathrm{s}$)
235	0.007	4000	4060	30
1180	0.036	4000	4230	145
2160	0.066	4000	4510	265

Fig. 4. Dark-signal of a pixel exhibiting a 4-level DC-RTS behavior after irradiation. The absence of transitions between the two intermediate levels indicates that there are two bi-level RTS centers involved [20].

Results presented in this section strongly suggest that the empirical model introduced in [12] is still valid at the $\mu\mathrm{m}^{3}$ scale and in another type of pixel design. Moreover, no significant Total Ionizing Dose (TID) contribution is identified in these test conditions.

IV. DC-RTS STUDY

A set of measurements of the DC-RTS behavior of the sensor was made prior to irradiation and only 8 RTS pixels over 2.25 megapixels investigated were detected at room temperature with an integration time of 1 s. This result shows that there are barely any bulk RTS centers and that the passivation of the interfaces is of good quality. In reality, bulk and interface RTS defects may exist, but if they do, they are hidden by the readout noise of the sensor and cannot be detected. An example of the RTS trace of a pixel exhibiting two bi-level defects is presented in Fig. 4. Black clamping is not an issue when probing DC-RTS since images are taken with a fixed integration time, which means a constant correction that can be seen as an offset.

A. Maximum transition amplitudes

After irradiation, DC-RTS maximum transition amplitudes between two successive discrete levels have been shown to be
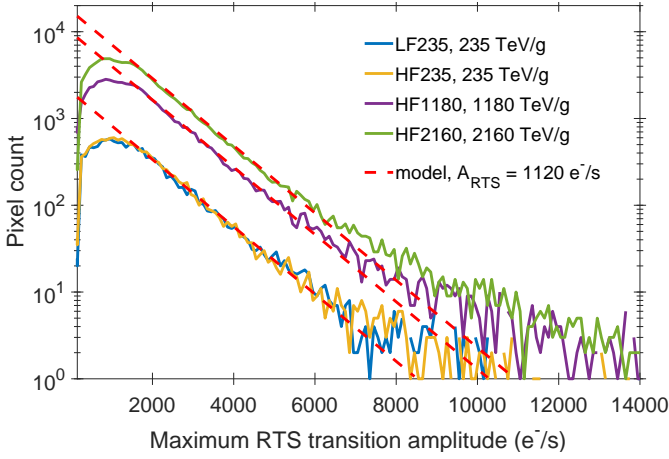
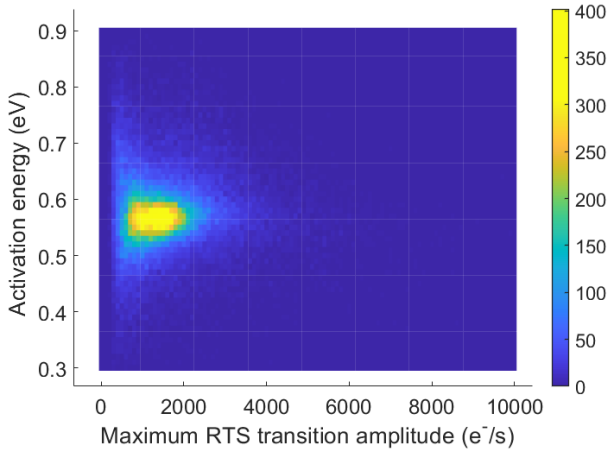Fig. 5. RTS Maximum transition amplitudes histogram at 22 °C.

Fig. 6. Distribution of the activation energy of the maximum RTS transition amplitude. The color scale represents the number of pixels per bin.

TABLE III
RTS MAXIMUM AMPLITUDE MODEL PARAMETERS

Sensor	A_{RTS} (e$^-$/s)	$K_{\mathrm{RTS}}V_{\mathrm{dep}}$ (center.(MeV/g)$^{-1}$)
LF235	1120	42
HF235	1120	42
HF1180	1120	42
HF2160	1120	41

data are shown in Table III, where results show very good agreement with the literature. Regarding the concentration of RTS defects, because the exact value of the depletion volume is not known, the values of the product $K_{\mathrm{RTS}}V_{\mathrm{dep}}$ are reported in Table. III. A volume range of 1 to $1.62\,\mu\mathrm{m}^3$ (the maximum pixel volume calculated in Section II) gives a K_{RTS} range of 26 to $42\,\mathrm{centers.cm}^{-3}.(\mathrm{MeV/g})^{-1}$ which is also in line with the literature. Working the other way around, using the typical value $K_{\mathrm{RTS}} \approx 30-35\,\mathrm{centers.cm}^{-3}.(\mathrm{MeV/g})^{-1}$ gives $V_{\mathrm{dep}} \approx 1.2-1.4\,\mu\mathrm{m}^3$ which is reasonable given the dimensions of the pixel and matches the volume of $1.28\,\mu\mathrm{m}^3$ used to make the best fit possible for dark current amplitudes in the previous section.

As with the dark current histograms, the highest amplitudes in the maximum RTS transition histogram are drifting away from the purely exponential distribution, especially for the high values of DDD. This behavior for highest amplitudes, has been reported previously in other CIS, and is confirmed here thanks to the high number of investigated pixels that increases the statistical likelihood of seeing these rarer events. This behavior can be partly explained by a local enhancement mechanism such as Electric-Field Enhancement (EFE) [17], [18], [19] as indicated in section III. To investigate this population of pixels, additional DC-RTS measurements were made at 12, 17, 27, and 47 °C to extract the activation energy of the maximum RTS amplitude per pixel. Fig. 6 displays the distribution of the activation energy of the maximum RTS transition amplitude. A mean activation energy of $0.57\pm0.08\,\mathrm{eV}$ is found for amplitudes below $6000\,\mathrm{e}^-/\mathrm{s}$. This activation energy is the signature of RTS centers located not far from the mid-gap of silicon and has been reported multiple times in previous studies (see section III.C in [20] for examples). For maximum RTS amplitudes over $6000\,\mathrm{e}^-/\mathrm{s}$, the mean activation energy is $0.51\pm0.09\,\mathrm{eV}$. This lowering of the activation energy for high maximum RTS amplitudes is in keeping with a generation rate that is enhanced by the electric field through Poole–Frenkel Barrier Lowering or Trap-Assisted Tunneling [15], [21].

Results presented in this section show that the physical behavior of RTS is still the same, even after reducing the volume of interest a hundred times. The result also indicates the validity of the semi-empirical model for maximum RTS amplitude at the $\mu\mathrm{m}^3$ scale in a new pixel design. As for the dark-current degradation, no evidence of TID-induced RTS is detected, but it may be hidden by the readout noise although the highest TID performed in this work, 90 krad, may or may not lead to TID induced DC-RTS in a planar PPD with a properly accumulated transfer gate, based on its design [22], [23], [24].

exponentially distributed [11]. This semi-empirical model is represented by the following discrete function,

$$F(X_k) = \frac{\mathrm{N_{pix}}.B.DDD.K_{\mathrm{RTS}}.V_{\mathrm{dep}}}{A_{\mathrm{RTS}}}\exp(-\frac{X_k}{A_{\mathrm{RTS}}}),\quad (7)$$

with $\mathrm{N_{pix}}$ the total number of pixels, B the bin size of the histogram, DDD the deposited displacement damage dose, $\mathrm{V_{dep}}$ the depletion volume per pixel, $\mathrm{A_{RTS}}$ the mean maximum transition amplitude and $\mathrm{K_{RTS}}$ a damage factor evaluating the number of DC-RTS centers created per unit of depleted volume and DDD. $\mathrm{A_{RTS}}$ and $\mathrm{K_{RTS}}$ factors are also found to be independent of design, technology, and particle type with the following typical values in CCDs and CISs at room temperature ($\approx 22\,°C$): $\mathrm{A_{RTS}} \approx 1200\,\mathrm{e\text{-}/s}$ and $\mathrm{K_{RTS}} \approx 30-35$ $\mathrm{centers.cm}^{-3}.(\mathrm{MeV/g})^{-1}$ [11], [16].

Fig. 5 shows the obtained maximum transition amplitude distributions for sensors LF235, HF235, HF1180 and HF2160. It can be seen that the amplitudes are exponentially distributed, as reported in numerous previous studies, despite the new low scale of the micro-volumes studied in this work. In addition, no flux effect can be seen when comparing sensors LF235 and HF235. The extracted slopes from experimental
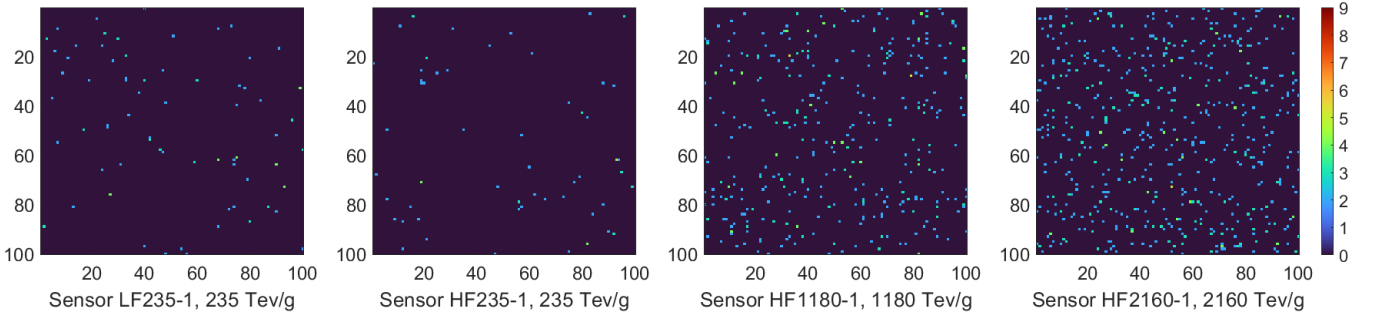
Fig. 7. Mapping of the detected RTS pixels in a ROI of 100*100 pixels for sensors LF235, HF235, HF1180 and HF2160. The colorbar represents the number of RTS levels.

TABLE IV
RTS PIXEL DETECTION IN A ROI OF 1500×1500 PIXELS

Sensor	DDD (TeV/g)	N_{RTS}	%RTS	%ML$_{\mathrm{RTS}}$	p$_{\mathrm{RTS}}$/p+ /pixel
LF235	235	13,589	0.60	24.5	$6.69{\times}10^{-6}$
HF235	235	14,511	0.64	23.6	$7.14{\times}10^{-6}$
HF1180	1180	71,460	3.18	27.1	$7.03{\times}10^{-6}$
HF2160	2160	115,678	5.14	25.0	$6.21{\times}10^{-6}$
CIS3 [25]	240	23,344	39	50	$4.39{\times}10^{-6}$
IC4-10µm-14MeV-n [26]	182	-	32	43	-
IC5-10µm-14MeV-n [26]	365	-	70	53	-
CIS6-11.2µm-50MeV-p [27]	270	200	20	-	$2.22{\times}10^{-6}$
CIS6-11.2µm-50MeV-p [27]	776	450	44	-	$1.75{\times}10^{-6}$

B. RTS levels and probability

Fig. 7 presents the mapping of the RTS levels for a sub-region of 100×100 pixels for sensors LF235, HF235, HF1180 and HF2160. As expected, more RTS pixels are created as more DDD is deposited. Table IV presents from left to right the sensor identification, the associated DDD deposited, the number of RTS pixels detected, the percentage of pixels with RTS, the proportion of multi-level RTS pixels in the whole population, and finally the probability of producing an RTS defect per incident proton and pixel. This latter probability has been introduced by Hopkins and Hopkinson in [2] and is expressed as follow:

$$p_{\mathrm{RTS}} = \frac{N_{\mathrm{RTS}}}{N_{\mathrm{pix}}.(A_{\mathrm{pix}}\phi)} \qquad (8)$$

where N_{pix} is the total number of pixels, N_{RTS} is the number of RTS pixels, A_{pix} is the pixel area, and ϕ is the fluence. These data are extracted for each sensor from the same 1500×1500 pixel Region Of Interest (ROI) used to trace previous amplitude distributions. The number of detected RTS pixels increases almost linearly with the DDD ($\approx 2.5 \times 10^{-3}$ %(TeV/g)$^{-1}$). On the other hand, the fraction of bi-level RTS pixels detected does not seem to vary much when the DDD increases. To put these results in perspective,

Table IV also presents a comparison with results extracted from previous studies. One of the studies uses 11 µm pitch BSI CIS irradiated to 240 TeV/g with 60 MeV protons [25]. Given that the irradiation profiles and measurement conditions (24 °C after 8 weeks of room temperature storage) for CIS3 in [25] and sensor LF235 and HF235 are very similar, it can be seen that the pixel pitch and the size of the depletion volume have a significant impact on the fraction of pixels exhibiting an RTS behavior, on the fraction of multi-level RTS pixels, as well as on the probability of producing an RTS defect per incident proton and pixel, as expected when looking at (8). However, the pixel area A_{pix} alone doesn't account for the variation of p_{RTS} observed here between small and large pixels. For CIS3, this probability should be roughly 100 times smaller than for LF235 and HF235, but it is here found to be only 1.6 times smaller. The significant lowering of %RTS when reducing pixels dimensions also affects p_{RTS}, and is the interest of the final subsection.

C. Pixel scaling

In this subsection, the effect of scaling the pixel's sensitive volume is discussed in order to have a look at its impact on the parameters presented in Table IV. Results indicate that no new effects are observed using small pixels and that the discrepancies observed in Table IV are only due to the reduction of the sensitive volume.

To obtain these results, three methods have been explored. Two of them use data from this study's small pixels to create artificially larger pixels. The third one uses the Poisson statistic to try to evaluate the fraction of RTS pixels in a sensor based on its sensitive volume and the DDD.

First, artificial bins of 12×12 pixels of sensor LF235 are made to create "macro" pixels whose total sensitive silicon volume matches the volume of $2.0{\times}10^{-10}$ cm^3 of the pixels of CIS3 in [25]. Two ways of creating such macro pixels are presented here.

The first, "SUM", consists in summing all of the pixels' temporal responses in every 12×12 sub-region. The edge-detection algorithm is then run on the newly created array containing the artificial macro pixels.

The second, "AGG", consists in aggregating the results obtained by the edge detection algorithm on single 1.12 µm pitch pixels. Using the AGG method, a macro pixel is considered
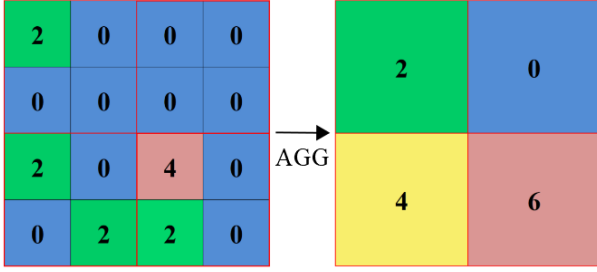
Fig. 8. Illustration of the effects of the AGG method on the resulting mapping of the number of RTS levels.

TABLE V
RTS PIXEL DETECTION IN SENSOR LF235 WITH ARTIFICIAL PIXEL SCALING

Sensor	V_{dep} μm^3	%RTS	$\%ML_{RTS}$	p_{RTS}/p + /pixel
LF235	1.28	0.60	24.5	6.69×10^{-6}
LF235 SUM	185	43	27	3.29×10^{-6}
LF235 AGG	185	57	53	4.42×10^{-6}
CIS3 [25]	200	39	50	4.39×10^{-6}

TABLE VI
MEAN READOUT NOISE (RMS) BEFORE AND AFTER IRRADIATION AND WHEN SUMMING 12×12 TEMPORAL PIXEL RESPONSES

DDD (TeV/g Si)	Readout noise (ADU)	Readout noise SUM 12×12 (ADU)
0	1.87	7.31
235	2.10	13.04
1180	2.27	27.77
2160	3.27	33.8

multi-level if the total sum of all the levels for each pixel in the sub-region is greater than two. An example of the way the AGG method operates is represented in Fig. 8.

Fig. 9 shows a map of the detected RTS pixels for a 120×120 classical pixel ROI of sensor LF235 along with the corresponding 10×10 ROI obtained using the two methods. Table V presents from left to right the percentage of RTS pixels, the fraction of multi-level RTS pixels, as well as the probability of producing an RTS defect per incident proton and pixel, after the pixel scaling for the two methods. Values from sensor LF235 and CIS3 [25] are also reported for comparison purposes. By comparing the two maps created with macro pixels, it can be seen that a few RTS pixels are not detected using the SUM method. This observation is confirmed when looking at the statistics on the whole array in Table V. The increase of the noise when adding all the elementary signals, shown in Table VI, could explain why some low amplitude RTS pixels are not detected by the algorithm, thus explaining the difference between the fraction of RTS pixels detected between the SUM and the AGG method. It can also be seen that the fraction of multi-level RTS pixels is also quite different for the two methods. A visual inspection of the resulting RTS traces and their reconstruction by the detection algorithm revealed that the algorithm would often miss several levels in SUM noisy traces. The SUM method thus does not seem very effective to create macro pixels of a large scale.

The disparity between %RTS determined with the AGG method and effectivly measured in [25] for CIS3 also needs to be discussed. The low maximum RTS amplitude detection threshold visible at around $1800\,e^-/s$ in Fig. 5 could explain this result. This threshold value depends on the detection algorithm used as well as on the sensor's noise performance. The threshold also determines the number of low amplitude RTS pixels included in the empirical model while missed by the detection algorithm. If the fraction of missed low amplitude

RTS pixels due to this threshold is smaller for LF235 than for CIS3, then having more RTS pixels after the AGG scaling is expected. Nonetheless, both the value of %RTS and p_{RTS} follow the good trend when increasing the pixel volume and the good orders of magnitude are retrieved. It shows that the variations observed in Table IV are essentially due to the small silicon sampling used in this work.

Regarding $\%ML_{RTS}$, the result obtained using the AGG method is in very good agreement with the result obtained in [25] for CIS3. This indicates that when increasing the pixel sensitive volume, the resulting increase of the fraction of multi-level RTS is mainly caused by the superposition of bi-level RTS centers in a single pixel.

To further investigate the effect of scaling the pixel's sensitive volume on %RTS, the Poisson statistic can be used in a way that is similar to what has been presented in Section III.B. Using the damage factor K_{RTS} the mean number of RTS centers per pixel can be expressed as

$$\mu_{RTS} = K_{RTS}V_{dep}DDD. \qquad (9)$$

Then, the probability of having n RTS centers in a pixel is given by

$$\mathcal{P}(n, \mu_{RTS}) = \frac{\mu_{RTS}^{n}}{n!}\exp(-\mu_{RTS}). \qquad (10)$$

Because a pixel will exhibit an RTS behavior as long as it contains at least one RTS center, the fraction of RTS pixels can then be calculated as

$$\%RTS_{\mathcal{P}} = 100 \times (1 - \mathcal{P}(0, \mu_{RTS})). \qquad (11)$$

Fig. 10 shows the calculated fraction of RTS pixels, $\%RTS_{\mathcal{P}}$, along with the empirically measured fraction of RTS pixels, %RTS, for this study's sensors and sensor CIS3 from [25]. Although $\%RTS_{\mathcal{P}}$ always overestimates the measurements, which is expected because of the detection threshold, it can be seen that the Poisson statistic corroborates the fact that %RTS increases when the mean number of RTS centers per pixel increases.

The relative error between %RTS and $\%RTS_{\mathcal{P}}$ is smaller for LF235 than for CIS3 ($\approx 30\%$ versus $\approx 50\%$ respectively). This difference supports the reason for the disparity between the fraction of RTS pixels detected with the AGG method and for CIS3 discussed before. In order to make sure that the AGG method is in line with the Poisson statistics, an artificial map that contains exactly the fraction of RTS pixels obtained using (11) with $\mu_{RTS} = 0.01$ (same mean number of RTS centers as LF235) is scaled using the AGG method, still using 12×12 pixel subgroups. Such macro pixels should contain 1.3 RTS
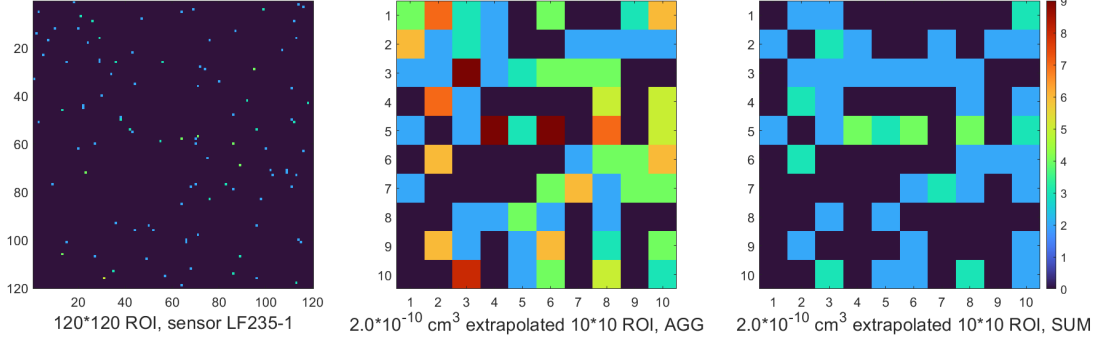
Fig. 9. 120×120 pixels ROI of sensor LF235 and corresponding 10 × 10 ROIs obtained using the AGG and SUM method on 12×12 pixels subgroups. The colorbar represents the number of RTS levels.
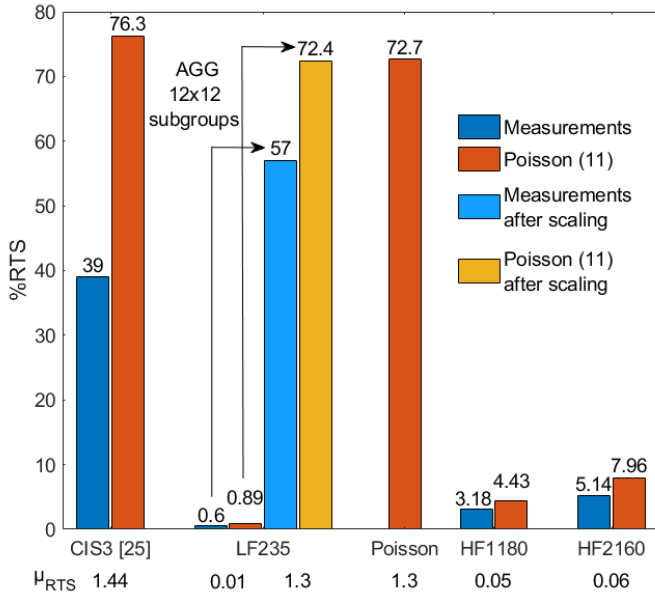

Fig. 10. Comparison between the measured and calculated fraction of RTS pixels for sensors LF235, HF1180, HF2160 and CIS3 from [25]. Are also reported $\%RTS_{\mathcal{P}}$ calculated using (11) with $\mu_{RTS} = 1.3$ and the fraction of RTS pixels measured in two maps scaled from $\mu_{RTS} = 0.01$ to $\mu_{RTS} = 1.3$ using the AGG method on 12×12 pixel subgroups.

centers. $\%RTS_{\mathcal{P}}$ is then evaluated using (11) with $\mu_{RTS} = 1.3$ and compared on Fig. 10 with the fraction of RTS detected in the map of macro pixels previously created. It can be seen that the AGG method replicates almost perfectly the effect of the increase of the mean number of RTS centers per pixel due to the volume scaling on the fraction of detected RTS. This result strengthens the analysis previously made and allows the conclusion that the discrepancy in $\%RTS$ observed between the very small pixels of this study and larger pixels of previous studies (Table IV) is due to the mean number of RTS centers per pixel being larger for pixels with a larger sensitive volume, at a given DDD, as seen in (9).

V. CONCLUSION

Proton induced dark current and DC-RTS were studied in a $1.12\,\mu m$ pitch COTS CIS. Despite some on chip corrections, the classical exponential tail of hot pixels is observed.

Measurements were compared to the empirical model first presented in [12] and the trends are still followed despite the changes in scale and pixel design. As expected, significant variations in the number of RTS pixels, RTS levels, and maximum transition amplitudes were detected in this irradiated COTS CIS. It shows that these defects should be taken into account when characterizing COTS CIS radiation hardness. The fitting of the experimental data allows extraction of the DC-RTS maximum-amplitude distribution' associated exponential slopes and damage factors. Even with the new scale silicon sampling, the values of A_{RTS} and K_{RTS} found in this work are well in line with the values found in the literature ($A_{RTS} \approx 1200$ e-/s at $\approx 22\,°C$ and $K_{RTS} \approx 30 - 35\,centers.cm^{-3}.(MeV/g)^{-1}$) for a wide range of image sensor technology nodes, designs, or pixel size. This result strengthens the idea of a universal behavior of the DC-RTS in silicon and shows that the tools created to study DC-RTS are still valid in COTS CIS at this scale.

No clear TID contribution is detected for both dark current and DC-RTS under the irradiation and measurements' condition even though TID also produces interface traps that can contribute to excess dark current. Such effects may appear at higher TID due to charge buildup in the pixel's surrounding oxides. It should also be reminded that the irradiation campaign was conducted with all sensors being grounded which is usually not the worst-case scenario to test the TID sensibility of CIS.

The influence of the size of the sensitive volume of a pixel on DC-RTS is also discussed. Results show that the proportion of RTS pixels and the proportion of multi-level RTS are lower when using a small pixel pitch. The order of magnitude of these parameters considering pixels with a larger pitch can be retrieved by scaling the results of this study. It demonstrates that the observed variations are only due to an increasing mean number of RTS centers per pixel when increasing the depletion volume.

Finaly, the shrinking pixel size of COTS CIS represents a good opportunity to study displacement damage effects in irradiated silicon, thanks to the very high statistic it offers. However, care should be taken because the increasing concentration of dopants [28] in recent submicron technologies might induce more severe EFE effects.

References

[1] I. H. Hopkins and G. R. Hopkinson, "Random telegraph signals from proton-irradiated CCDs," *IEEE Trans. Nucl. Sci.*, vol. 40, no. 6, pp. 1567–1574, Dec. 1993.

[2] I. Hopkins and G. Hopkinson, "Further measurements of random telegraph signals in proton irradiated CCDs," *IEEE Trans. Nucl. Sci.*, vol. 42, no. 6, pp. 2074–2081, Dec. 1995.

[3] M. Beaumel, D. Hervé, and D. Van Aken, "Cobalt-60, proton and electron irradiation of a radiation-hardened active pixel sensor," *IEEE Trans. Nucl. Sci.*, vol. 57, no. 4, pp. 2056–2065, Aug. 2010.

[4] E. R. Fossum and D. B. Hondongwa, "A review of the pinned photodiode for CCD and CMOS image sensors," *IEEE J. Electron Devices Soc.*, vol. 2, no. 3, pp. 33–43, May 2014.

[5] J. Ahn *et al.*, "A 1/4-inch 8mpixel CMOS image sensor with 3D backside-illuminated 1.12 μm pixel with front-side deep-trench isolation and vertical transfer gate," in *Proc. International Solid-State Circuits Conference Dig. Tech.*, San Francisco, CA, USA, 9-13 Feb. 2014, pp. 124–125.

[6] S. Sukegawa *et al.*, "A 1/4-inch 8mpixel back-illuminated stacked CMOS image sensor," in *Proc. International Solid-State Circuits Conference Dig. Tech.*, San Francisco, CA, USA, 17-21 Feb. 2013, pp. 484–485.

[7] R. Matthews, N. Falkner, and M. Sorell, "Reverse engineering the Raspberry Pi Camera V2: A study of pixel non-uniformity using a scanning electron microscope," *Forensic Sci. Int.: Digital Investigation*, vol. 32, March 2020, Art. no. 200900.

[8] B. Pain and B. R. Hancock, "Accurate estimation of conversion gain and quantum efficiency in CMOS imagers," in *Sensors and Camera Systems for Scientific, Industrial, and Digital Photography Applications IV*, vol. 5017, Santa Clara, CA, USA, 16 May 2003, pp. 94–103.

[9] G. P. Summers, E. A. Burke, P. Shapiro, S. R. Messenger, and R. J. Walters, "Damage correlations in semiconductors exposed to gamma, electron and proton radiations," *IEEE Trans. Nucl. Sci.*, vol. 40, no. 6, pp. 1372–1379, Dec. 1993.

[10] L. Standaert, N. Postiau, and M. Loiselet, "UCL irradiation facilities status," in *17th European Conference on Radiation and Its Effects on Components and Systems (RADECS)*, Geneva, Swtizerland, 2-6 Oct. 2017, pp. 261–263.

[11] V. Goiffon, G. R. Hopkinson *et al.*, "Multilevel RTS in proton irradiated CMOS image sensors manufactured in a deep submicron technology," *IEEE Trans. Nucl. Sci.*, vol. 56, no. 4, pp. 2132–2141, Aug. 2009.

[12] C. Virmontois, V. Goiffon, P. Magnan, S. Girard, O. Saint-Pe, S. Petit, G. Rolland, and A. Bardoux, "Similarities between proton and neutron induced dark current distribution in CMOS image sensors," *IEEE Trans. Nucl. Sci.*, vol. 59, no. 4, pp. 927–936, Aug. 2012.

[13] J. Srour and D. Lo, "Universal damage factor for radiation-induced dark current in silicon devices," *IEEE Trans. Nucl. Sci.*, vol. 47, no. 6, pp. 2451–2459, Dec. 2000.

[14] J.-M. Belloir, V. Goiffon, C. Virmontois, M. Raine, P. Paillet, O. Duhamel, M. Gaillardin, R. Molina, P. Magnan, and O. Gilard, "Pixel pitch and particle energy influence on the dark current distribution of neutron irradiated CMOS image sensors," *Opt. Express*, vol. 24, no. 4, pp. 4299–4315, Feb. 2016.

[15] J. Bogaerts, B. Dierickx, and R. Mertens, "Enhanced dark current generation in proton-irradiated CMOS active pixel sensors," *IEEE Trans. Nucl. Sci.*, vol. 49, no. 3, pp. 1513–1521, June 2002.

[16] C. Virmontois, V. Goiffon, M. S. Robbins, L. Tauziède, H. Geoffray, M. Raine, S. Girard, O. Gilard, P. Magnan, and A. Bardoux, "Dark Current Random Telegraph Signals in Solid-State Image Sensors," *IEEE Trans. Nucl. Sci.*, vol. 60, no. 6, pp. 4323–4331, Dec. 2013.

[17] M. S. Robbins and L. G. Rojas, "An assessment of the bias dependence of displacement damage effects and annealing in silicon charge coupled devices," *IEEE Trans. Nucl. Sci.*, vol. 60, no. 6, pp. 4332–4340, Dec. 2013.

[18] O. Gilard *et al.*, "Statistical analysis of random telegraph signal maximum transition amplitudes in an irradiated CMOS image sensor," *IEEE Trans. Nucl. Sci.*, vol. 61, no. 2, pp. 939–947, April 2014.

[19] A. Le Roch *et al.*, "Radiation-induced leakage current and electric field enhancement in CMOS image sensor sense node floating diffusions," *IEEE Trans. Nucl. Sci.*, vol. 66, no. 3, pp. 616–624, March 2019.

[20] C. Durnez, V. Goiffon, C. Virmontois, J.-M. Belloir, P. Magnan, and L. Rubaldo, "In-depth analysis on radiation induced multi-level dark current random telegraph signal in silicon solid state image sensors," *IEEE Trans. Nucl. Sci.*, vol. 64, no. 1, pp. 19–26, Jan. 2017.

[21] L. Kleinman, "Theory of phonon-assisted tunneling in semiconductors," *Phys. Rev.*, vol. 140, no. 2A, pp. A637–A648, Oct. 1965.

[22] V. Goiffon, M. Estribeau, O. Marcelot, P. Cervantes, P. Magnan, M. Gaillardin, C. Virmontois, P. Martin-Gonthier, R. Molina, F. Corbiere, S. Girard, P. Paillet, and C. Marcandella, "Radiation effects in pinned photodiode CMOS image sensors: Pixel performance degradation due to total ionizing dose," *IEEE Trans. Nucl. Sci.*, vol. 59, no. 6, pp. 2878–2887, Dec. 2012.

[23] V. Goiffon, C. Virmontois, P. Magnan, P. Cervantes, S. Place, M. Gaillardin, S. Girard, P. Paillet, M. Estribeau, and P. Martin-Gonthier, "Identification of radiation induced dark current sources in pinned photodiode CMOS image sensors," *IEEE Trans. Nucl. Sci.*, vol. 59, no. 4, pp. 918–926, Aug. 2012.

[24] V. Goiffon, M. Estribeau, P. Cervantes, R. Molina, M. Gaillardin, and P. Magnan, "Influence of transfer gate design and bias on the radiation hardness of pinned photodiode CMOS image sensors," *IEEE Trans. Nucl. Sci.*, vol. 61, no. 6, pp. 3290–3301, Dec. 2014.

[25] B. Liu *et al.*, "Study of dark current random telegraph signal in proton-irradiated backside illuminated CMOS image sensors," *Results Phys.*, vol. 19, Dec. 2020, Art. no. 103443.

[26] C. Virmontois, V. Goiffon, P. Magnan, O. Saint-Pé, S. Girard, S. Petit, G. Rolland, and A. Bardoux, "Total ionizing dose versus displacement damage dose induced dark current random telegraph signals in CMOS image sensors," *IEEE Trans. Nucl. Sci.*, vol. 58, no. 6, pp. 3085–3094, Dec. 2011.

[27] C. Virmontois, C. Durnez, M. Estribeau, P. Cervantes, B. Avon, V. Goiffon, P. Magnan, A. Materne, and A. Bardoux, "Radiation Effects in Pinned Photodiode CMOS Image Sensors: Variation of Epitaxial Layer Thickness," *IEEE Trans. Nucl. Sci.*, vol. 64, no. 1, pp. 38–44, Jan. 2017.

[28] M. Uchiyama *et al.*, "A 40/22nm 200mp Stacked CMOS Image Sensor with 0.61um Pixel," in *2021 International Image Sensor Workshop (IISW)*, Online Conference, 20-23 Sept 2021, Art. no. R02.